

ripple: Differentiable Waveforms for Gravitational Wave Data Analysis



ADAM COOGAN,^{1,2} THOMAS D. P. EDWARDS,^{3,4,5} DANIEL FOREMAN-MACKEY,⁶ MAXIMILIANO ISI,⁶ KELVIN K. H. TAM,^{6,7}
KAZE W. K. WONG,⁶ AND AARON ZIMMERMAN⁸

¹*Département de Physique, Université de Montréal, 1375 Avenue Thérèse-Lavoie-Roux, Montréal, QC H2V 0B3, Canada*

²*Mila – Quebec AI Institute, 6666 St-Urbain, #200, Montreal, QC, H2S 3H1*

³*William H. Miller III Department of Physics and Astronomy, Johns Hopkins University, Baltimore, Maryland 21218, USA*

⁴*The Oskar Klein Centre, Department of Physics, Stockholm University, AlbaNova, SE-106 91 Stockholm, Sweden*

⁵*Nordic Institute for Theoretical Physics (NORDITA), 106 91 Stockholm, Sweden*

⁶*Center for Computational Astrophysics, Flatiron Institute, New York, NY 10010, USA*

⁷*Department of Physics, The Chinese University of Hong Kong, Shatin, N.T., Hong Kong*

⁸*Center for Gravitational Physics, University of Texas at Austin, Austin, TX 78712, USA*

ABSTRACT

Since their discovery in 2015, gravitational waves (GWs) have developed into a unique observational probe used throughout fundamental and astro-physics. As more detections continue, data analysis tasks are becoming increasingly computationally demanding. Here we propose the use of automatic differentiation through the programming framework **JAX** for accelerating a variety of these analysis tasks. Firstly, we demonstrate that highly accurate waveforms (IMRPhenomD) can be written in **JAX** and demonstrate that the evaluation speed of the waveform (and its derivative) is not substantially slower than the **lalsuite** implementation in C++. We then focus on three applications where speed and differentiable waveforms are essential. Firstly, we demonstrate that stochastic gradient descent can be used to optimize the ~ 200 coefficients that make up the waveform. In particular, we demonstrate that the typical *match* with numerical relativistic waveforms can be improved by more than 30% without any additional overhead. Secondly, we show that Fisher forecasting calculations can be sped up by $\sim 100\times$ with no loss in accuracy. This increased speed makes population forecasting substantially simpler, as discussed extensively in (Iacovelli et al. 2022a,b). Finally, we show that gradient based samplers like Hamiltonian Monte Carlo can improve acceptance rates of MCMC. Since differentiable waveforms appear to have substantial advantages for a variety of tasks throughout GW science (with little downside), we propose that waveform developers use **JAX** to build new waveforms moving forward. Our waveform code, called **ripple**, can be found at XXX, and will continue to be updated with new waveforms as they are formulated.

1. INTRODUCTION

The discovery of gravitational waves (GWs) from inspiraling and merging compact objects (COs) has revolutionized our understanding of both fundamental physics and astronomy (Abbott et al. 2021). Although the data volumes from GW detectors are relatively small, analyzing the data is a computationally demanding task. In addition, this computational cost will substantially increase when next generation detectors come online. The complexity begins before data gathering where one is required to generate banks of template waveforms which will be used for a matched-filter search (Owen & Sathyaprakash 1999; Owen 1996). Once potential candidates are found, parameter estimation (PE) is performed to extract the detailed source properties of each event. In the most minimal example,

this requires a Markov Chain Monte Carlo (MCMC) on an 11 dimensional parameter space for each event. Beyond this simple scenario, more complex waveform models with many additional parameters may be used to test for deviations from General Relativity. Finally, using the results of the PE, population synthesis models constrain the progenitors systems from which the black holes we see merging today began their journey (Wong et al. 2022). All of these tasks require significant compute. In this paper, we will argue that differentiable waveforms (and more generally differentiable pipelines) can play a significant role in alleviating this computational demand.

Derivatives are ubiquitously useful throughout data analysis tasks. For instance, during PE, derivative information can be used to guide the sampling towards re-

gions with higher likelihood values (e.g. in Hamiltonian Monte Carlo (Betancourt 2017) or Gradient Descent). Gradients are particularly valuable for high dimensional spaces. Unfortunately, in the field of GW data analysis, analytic derivatives of the necessary quantities (such as the likelihood) have historically been difficult to obtain. Numerical derivatives also suffer from accuracy issues stemming from rounding or truncation errors. However, recent progress in automatic differentiation (AD) has shown promise in allowing general, fast derivative calculations for gravitational waveforms (Coogan et al. 2022b).

Automatic differentiation is a family of methods used to compute machine precision derivatives with little computational overhead. AD’s recent ascendance is primarily driven by its use in machine learning, particularly for derivative computations of neural networks which use gradient descent during training. The core idea of AD is that any mathematical function can be broken down into a small set of basic operations, each with a known differentiation rule.¹ The full derivative can then be constructed using the chain rule. There are now a variety of AD implementations, most notably in deep learning frameworks such as `pytorch` (Paszke et al. 2019) and `tensorflow` (Abadi et al. 2015). More general frameworks exist in `julia` (Innes 2018; Revels et al. 2016), although `julia`’s limited support in GW physics precludes its general use. Here we make use of `JAX` (Bradbury et al. 2018) due to its easy integration with `python` libraries and its just-in-time (JIT) compiler which allows the same code to run on a variety of hardware accelerators (i.e. GPUs).

There are a variety of gravitational waveforms currently used in analysis pipelines. They are generally structured into different families, the most common of which are: the effective-one-body (EOB), the phenomenological inspiral-merger-ringdown (IMRPhenom), and numerical relativity surrogate (NRsurrogate). Of these, the IMRPhenom family is most well suited for an AD implementation in `JAX`. In particular, its closed form expression and fixed size frequency grid make a `JAX` implementation that complies with the constraints of JIT compilation simple. EOB waveforms on the other hand require... **(TE: Max or Kaze, could one of you write something about why its hard? I don’t know enough about EOB.)**

In this paper we argue that differentiable waveforms will be a vital component for the future of GW data

analysis. In addition, we present `ripple`, a small GW `python` package which can serve as a repository for differentiable implementations of some of the main waveforms currently used in LIGO and Virgo analyses. The remainder of this paper is structured as follows. In Sec. 2 we discuss the differentiable waveforms implemented in `ripple` and perform some benchmarks to demonstrate the speed and accuracy of the derivative calculations. In Sec. 3 we discuss three distinct applications using differentiable waveforms. Firstly, we illustrate how the fit coefficients that form part of the IMRPhenom waveform models could be improved by high dimensional fitting, enabled by a differentiable waveform. Secondly, we implement differentiable detector response functions and show that the speed of Fisher matrix calculations can be substantially improved using AD. Finally, we run an illustrative injection example using Hamiltonian Monte Carlo to demonstrate that the acceptance rate of derivative samplers is substantially larger than traditional MCMCs. The associated code can be found at `ripple` (Coogan et al. 2022a).

2. DIFFERENTIABLE WAVEFORMS

A variety of waveform families have been developed to accurately model the GW emission from COs. When the COs are relatively well separated, the dynamics of the system can be well approximated with post-Newtonian expansion. However, close to merger, numerical relativistic simulations are required to accurately model the binary. Unfortunately, these numerical simulations are computationally expensive and cannot be run in conjunction with data analysis. Approximate, phenomenological waveforms have therefore been constructed to enable relatively fast waveform generation at sufficient accuracy.

As mentioned in the previous section, the three major waveform families that have been developed to date are: EOB, NRsurrogate, and IMRPhenom. Note that unlike NRsurrogate, both the EOB and PhenomIMR waveforms are calibrated to numerical relativity waveforms. EOB waveforms require one to model the binary system using a Hamiltonian and are typically slow to evaluate whereas IMRPhenom waveforms are constructed with simple closed-form expressions. IMRPhenom waveforms are therefore ideally suited for AD, especially using `JAX`. In this paper we focus mainly on the aligned spin circular orbit model IMRPhenomD (Husa et al. 2016; Khan et al. 2016).

The implementation of IMRPhenomD in `lalsuite` is in C, and therefore needs to be rewritten natively into `python` to be compatible with `JAX`. We have re-written IMRPhenomD from scratch using a combination of pure

¹ Of course, non-differentiable functions exist and care must be taken when treating these special cases.

`python` and `JAX` derivatives. In addition, we have restructured the code for readability and evaluation speed as well as exposing the internal fitting coefficients to the user (which we will use later in Sec. 3).

To demonstrate our implementation of IMRPhenomD is faithful to the `lalsuite` implementation, we start by defining the noise weighted inner product:

$$(h_{\theta_1}|h_{\theta_2}) \equiv 4 \operatorname{Re} \int_0^\infty df \frac{h_{\theta_1}(f)h_{\theta_2}^*(f)}{S_n(f)}, \quad (1)$$

where S_n is the (one-sided) noise power spectral density (PSD) and h_{θ_1} is the frequency domain waveform evaluated at the intrinsic parameter point θ_1 . We can then normalize the inner product through

$$[h_{\theta_1}|h_{\theta_2}] = \frac{(h_{\theta_1}|h_{\theta_2})}{\sqrt{(h_{\theta_1}|h_{\theta_1})(h_{\theta_2}|h_{\theta_2})}}. \quad (2)$$

Now we are ready to define the *match* which is given by

$$m(h_{\theta_1}|h_{\theta_2}) \equiv \max_{t_c, \phi_c} [h_{\theta_1}|h_{\theta_2}] \quad (3)$$

where t_c and ϕ_c are, respectively, the time and phase of coalescence.

Since the match is a measure of the difference between two waveforms, we can use it to demonstrate that the implementation of IMRPhenomD in `ripple` accurately matches the `lalsuite` implementation. This is shown in Fig. 1, where we have calculated the $m(h_{\theta_1}|\bar{h}_{\theta_1})$ across the entire parameter space.² Here, h_{θ_1} corresponds to the `ripple` waveform implementation and \bar{h}_{θ_1} is the `lalsuite` implementation. From Fig. 1, it is clear that the `ripple` waveform matches with the `lalsuite` waveform to numerical precision across the majority of the parameter space. In particular, the blue points indicate parameter points where the $1 - m(h_{\theta_1}|\bar{h}_{\theta_1}) = 0$ and would therefore not appear in the log scale colorbar.

There remains some slight deviation between the two waveform implementations at low total mass. **(TE: Do I need to look more into this...? The discussion below looks odd with this plot)** This is likely due to the fact that cubic interpolators, which are used within IMRPhenomD to calculate the ringdown and damping frequencies, are not currently supported in `JAX`. Instead, we initially use `scipy`'s cubic interpolator to create a fine grid of XXX values, which we then linearly interpolate during waveform generation. Unfortunately, we cannot make the initial cubic interpolation arbitrarily

² Specifically, we use 2000 points in the ranges $m_{1,2} = (1, 50) M_\odot$ and $\chi_{1,2} = (-1, 1)$. In addition, we evaluated the waveforms on a frequency grid from 32 Hz to 1024 Hz with frequency spacing $\Delta f = 0.0125$ Hz.

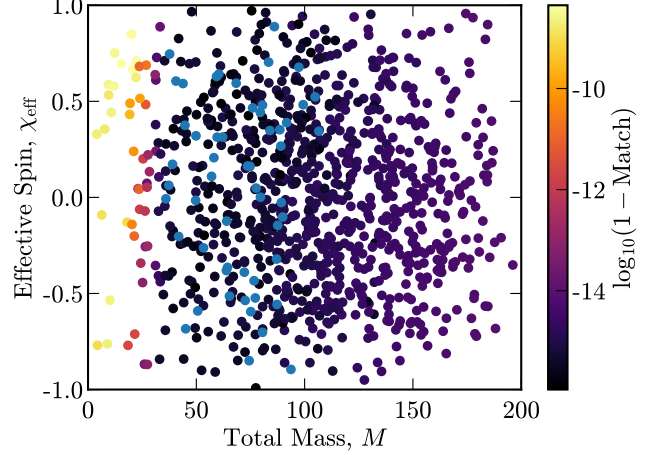


Figure 1. Match between the `ripple` and `lalsuite` implementations of the IMRPhenomD waveform as a function of total mass and effective spin. **(TE: Need to investigate more?)**

fine as this would add additional computational overhead when loading the data during waveform evaluation. The remaining error in the waveform at high masses is therefore primarily down to the coarseness in this interpolation. Note however, that the differences are well below the accuracy requirements of the waveforms and will have no noticeable for realistic data analysis tasks.

For maximum utility, a waveform needs to be fast to evaluate. Fortunately, the IMRPhenom waveforms are constructed from simple closed-form expressions which are computationally efficient. Since the `lalsuite` implementation of IMRPhenomD is written in `C`, the evaluation of the waveform itself is faster than `ripple`. Benchmarking on a MacBook Pro with an M1 Max Apple Silicon processor, we find that a single waveform evaluation takes $\sim 2 - 5$ ms for `lalsuite` (interfaced with `python`) and $\sim 5 - 8$ ms for `ripple`.³ Although slower on a CPU benchmark, a key advantage of using `JAX` is its native ability to run on a GPU. Waveform calls can therefore be evaluated in parallel, massively improving performance. Performing the same benchmark as above on a google colab notebook with the freely provided GPU, we find that on average waveform evaluations take ~ 0.00005 ms, nearly five orders of magnitude faster. Generalizing `lalsuite` waveforms to run on a GPU would be a significant undertaking.

³ For this benchmark we used 16 Hz and 1024 Hz for the lowest and highest frequencies respectively. In addition, we used a frequency spacing of 0.0125 Hz. We performed this benchmark by evaluating the waveform 5000 times and taking the average evaluation time.

The primary argument of this paper is that waveform derivatives will also be highly valuable to data analysis tasks. AD provides two big advantages when it comes to evaluating derivatives compared to numerical differentiation. First, the accuracy of derivatives from AD are significantly more stable than finite difference methods. In particular, finite differences suffer from both rounding and truncation errors, meaning that the user is required to *tune* the width over which the difference is taken. On the other hand, AD produces machine precision derivatives with no tuning. Second, AD scales favourably with the dimensionality of the function. In particular, for every input dimension, D , added one would need to evaluate the function at least $2D$ times to calculate finite difference derivatives for all input parameters. For reverse mode AD, one only needs two function calls to evaluate the derivative of all input parameters, regardless of dimension.⁴ Since the parameter space of GWs in General Relativity (GR) has $\mathcal{O}(10)$ dimensions, the speed of derivative evaluation is less crucial than the stability. However, this might change for waveforms in beyond GR models where many more parameters are added.

Overall, we have demonstrated that the IMRPhenom waveform family is ideally suited for AD. Moreover, we have shown that our implementation of IMRPhenomD in `ripple` is accurate and quick to evaluate, especially when hardware acceleration is available. In the next section, we will discuss a variety of potential use cases of differentiable waveforms.

3. APPLICATIONS

Here, we will illustrate how three core tasks in GW science can be substantially improved through the use of differentiable waveforms. In the paper we will primarily look at toy examples, leaving a more careful analyses to future work. The three tasks discussed here cover a wide range of GW science, starting with waveform development all the way to forecasting and parameter estimation.

3.1. *Finetuning Waveform Coefficients*

Having an accurate waveform model is essential for many data analysis tasks in GW, such as searching for signals and estimating source parameters given data. While waveforms generated using numerical relativity simulations are commonly regarded as the most accurate, they are too computationally expensive to be used

in any practical data analysis tasks. To create waveform models that can be used in data analysis, there are a number of groups creating “approximants” of the full numerical relativity waveforms, which are essentially simpler ansatzes that are only approximations but can be evaluated much faster.

Every waveform approximant has some fitting coefficients that are tuned during the process of calibrating the ansatz to NR waveforms. In the case of IMRPhenomD, there are 209 fitting coefficients used to capture the separate behavior of the amplitude and phase as a function of the mass ratio and spins. The accuracy of fitting coefficients determines how well the approximant reproduces the NR waveform. The inaccuracy in obtaining the fitting coefficients means misrepresentation of the NR waveform, which can translate to systematic error in downstream data analysis task. For example, sufficiently large systematic errors in the waveform would cause the recovered source parameters to be biased in the case of PE.

Previously in the construction of IMRPhenomD (Khan et al. 2016), waveform coefficients are fitted in segments with amplitude and phase separated. Furthermore, IMRPhenomD is divided in three fitting segments, inspiral, merger and ringdown. Each of these segments has their own set of fitting coefficients. After obtaining the fitting coefficient for individual segments, they are then “stitched” together such that they are continuous in the first derivative. The process of stitching introduces some addition inaccuracy in the waveform model, as the connections would affect the originally fitted segments. The coefficients of the current IMRPhenomD implementation are tuned in sub-sets of parameters instead of all together. This means the tuning process ignore the correlation between different sub-sets of parameters, so the best-fitted solution obtained by fitting sub-sets of parameters may not be the global optimum compared to fitting all coefficients at once. By jointly fitting all coefficients, the correlation in fitting individual and connecting different segments can be accounted during the optimization. Therefore, there is potential improvement of the accuracy by fitting all coefficients at once.

In general, optimization problems in a high dimensional space benefit from having access to the gradient of the objective function. Since we can differentiate through the entire waveform model against the fitting parameters, one can use gradient descent to find the optimal fitting parameters all at once instead of fitting them in subsets.

The first step in fitting all coefficients is to define a loss function that measures the goodness-of-fit of the

⁴ Note that although the number of function calls is small, reverse mode AD does add memory overhead. We’ve not found this to be limiting in any of the situations tested so far.

optimization procedure, which we choose it to be the mismatch between the NR waveform and the approximant waveform.

$$\mathcal{M}(\lambda) = 1 - m(h_{\text{IMR}}(\lambda)|h_{\text{NR}}(\lambda)), \quad (4)$$

where λ is a vector of the fitting coefficients, h_{IMR} is the waveform generated by the IMRPhenomD and h_{NR} is the waveform generated by the numerical relativity simulation. Given the loss function, we use gradient descent to find the optimal fitting coefficients.

$$\lambda \leftarrow \lambda - \alpha \nabla \mathcal{M}, \quad (5)$$

where α is the learning rate. We set α to be a very small number, i.e. 10^{-6} , since the initial guess already lies close to the desired optimum. We terminate the program after 30000 steps, in which λ has converged to the optimum.

As a demonstration, Fig. 2 shows the relative error of original and optimized waveform at different frequencies. In this optimization procedure, we took NR waveforms h_{NR} stated in (Khan et al. 2016) as training waveforms to fit waveform coefficients. We can see the error of optimized waveform is lower than that of the original waveform for most of the domain. In particular, the error in the early inspiral region is decreased by half while other regions also show good improvement in accuracy.

We can generalize the fitting procedure described above to a collection of waveforms. In that case, the loss function is defined as the average of the mismatch of individual waveforms, given by

$$\mathcal{L} = \frac{1}{N} \sum_{i=1}^N \mathcal{M}_i, \quad (6)$$

where \mathcal{M}_i is the mismatch of individual training waveforms and N is the total number of training waveforms used in optimization. This optimization is more difficult since we are applying the same set of coefficients to waveforms with different intrinsic parameters, such as mass ratio and spins. From Eq. 6, we can see the averaging between waveforms with different intrinsic parameters implies there are trade-off in performance in different regions of the intrinsic parameter space.

In Fig. 3, we show the distribution of log mismatches. One can see the distribution of mismatch after optimization has smaller mismatch compared to before optimization, showing the optimization improves the accuracy of the waveform model. While many waveforms improved their accuracy, some remain to have similar mismatches. This phenomenon is mainly due to the reduced spin approximation used in IMRPhenomD, where spin degeneracy is introduced, hence restricting further improvements. In an upcoming paper, we will give a detailed

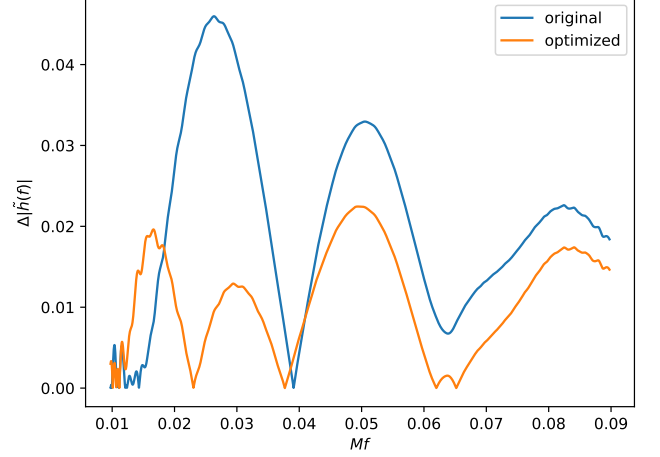


Figure 2. Relative error of IMRPhenomD waveform amplitudes. Blue: Error between original Phenom waveform and NR waveform; Orange: Error between optimized waveform and NR waveform.

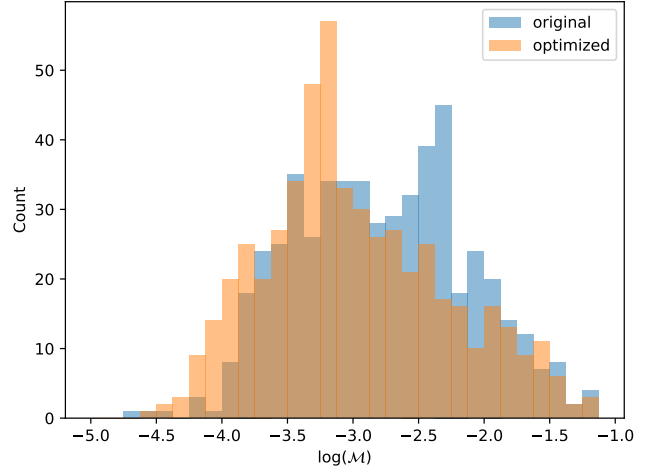


Figure 3. Distributions of log mismatches of testing waveforms. Blue: Original waveforms; Orange: Optimized waveforms.

discussion of how such an approximation scheme affects the optimization procedure. Nevertheless, the peak of the original waveform distribution moved to the left end of the distribution, indicating that the optimization procedure improved the model. Therefore, the new set of waveform coefficients can produce better waveforms for GW analyses.

3.2. Fisher Forecasting

Forecasting the sensitivity of future experiments is an essential task in GW science. Due to its theoretical simplicity and evaluation speed, the Fisher matrix formalism is commonly deployed to estimate how well a binary system's parameters can be measured. The Fisher

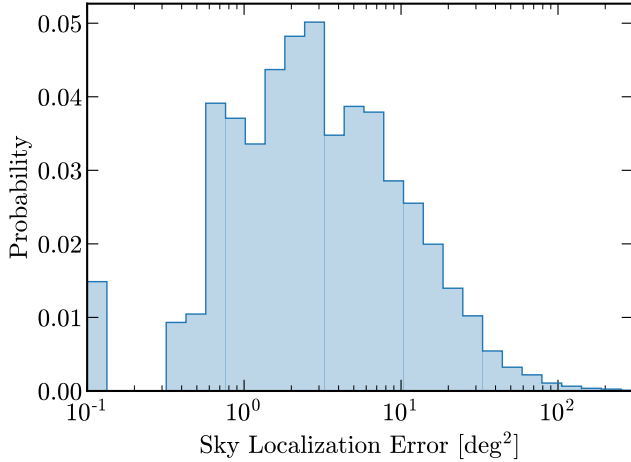


Figure 4. This plot should show a sky localization error bar.

matrix approach is built around the assumption of a Gaussian likelihood. Although in practice this assumption is often violated in real GW datasets, the results obtained using a Fisher analysis can provide quick and useful diagnostics in evaluating sensitivities for a variety of models and detector configurations.

Computing the Fisher matrix requires one to evaluate derivatives of the likelihood which in turn involves derivatives of the waveform model and detector projection functions. AD is therefore perfectly suited for computing Fisher matrices accurately and efficiently. Forecasting with Fisher matrices for third generation detectors has already been extensively explored in (Iacovelli et al. 2022a,b). Here we purely want to illustrate the simplicity and speed of AD for forecasting rather than providing new physics insights. We therefore consider a simple, three detector setup corresponding to the two LIGO detectors in addition to Virgo.

The Fisher information matrix for a single detector is typically given by

$$\mathcal{I}_{ij}^k = (\partial_i h_0 | \partial_j h_0), \quad (7)$$

where k indicates the detector, $\partial_i = \partial/\partial\theta_i$, and h_0 is the strain measured by the detector which is given by,

$$h_0(\theta) = F_+(\lambda)h_+(\phi) + F_\times(\lambda)h_\times(\phi). \quad (8)$$

Note that here we have separated out the intrinsic (ϕ) and extrinsic (λ) variables as well as introducing the detector projection functions for the plus and cross polarizations as F_+ and F_\times respectively. Since we are considering a three detector setup we simply add the Fisher matrices from the individual detectors to get the combined Fisher matrix:

$$\mathcal{I}_{ij} = \mathcal{I}_{ij}^{\text{Hanford}} + \mathcal{I}_{ij}^{\text{Livingston}} + \mathcal{I}_{ij}^{\text{Virgo}}. \quad (9)$$

m_1, m_2	$\mathcal{U}[1.0, 50] \text{ M}_\odot$
χ_1, χ_2	$[-0.99, 0.99]$
D	$[500, 1000] \text{ Mpc}$
t_c	0.0
ϕ_c	0.0
Inclination Angle, ι	$\mathcal{U}[0, 1]$
Polarization Angle, ψ	$\mathcal{U}[0, 1]$
Right Ascension, δ	$\mathcal{U}[0, 1]$
Declination, α	$\mathcal{U}[0, 1]$

Table 1. Priors for the 11 dimensional parameter space used for the Fisher forecasting population analysis in Sec. 3.2. \mathcal{U} indicates a uniform distribution between the two variables in the brackets.

Finally, we invert the Fisher matrix to calculate the covariance matrix.

To illustrate the computational speed of computing Fisher matrices with AD, we consider a population of binaries and compute the sky localization error following Eq. (28) in (Iacovelli et al. 2022a,b). Since the Fisher matrix approach is known to have both theoretical issues as well as numerical instabilities for low signal-to-noise events, we restrict our population to only nearby systems. A full list of the distributions used to generate the various parameters in our population are given in Tab. 1. The resulting population produces binaries with signal-to-noise ratios ranging from $\mathcal{O}(10 - 10^2)$.

The distribution of sky localization errors from a population of 10^3 binaries can be seen in Fig. 4. We have verified that our errors agree with a separate dedicated Fisher forecasting code (Borhanian 2021) to within X percent. This demonstrates that AD can be used to accurately produce population level forecasts.

Moreover, each error calculation (including computing the Fisher matrices for each detector and the inversion process) is substantially faster. In particular, we find that after compilation each error calculation takes approximately half a second on a single computing core. **GWbench** (Borhanian 2021), on the other hand, takes $\mathcal{O}(\text{minutes})$ for each Fisher calculation using the same detector setup and frequency grid. This factor of over 100 speed up is substantial considering the fact that a single core evaluation of the **ripple** waveform is slower than the **lalsuite** call. As discussed above, performance can be further improved by utilising hardware acceleration such as parallel GPU processing. AD therefore represents a fast and accurate way of performing population level analyses, and should be utilized for testing the capabilities of next generation detectors.

3.3. Derivative Based Samplers - Hamiltonian Monte Carlo

After the search algorithms have constructed a list of confidently detected binaries, the next step is to sample from the posterior of each sources parameters - so called parameter estimation (PE). To do this, one typically uses a Markov Chain Monte Carlo (MCMC) or nested sampler (Feroz et al. 2009; Speagle 2020). Although robust, both MCMC and nested sampling are slow to converge and are known to perform poorly in high dimensional parameter spaces. For example, sampling the 15 dimensional parameter space for a BBH system can take $\mathcal{O}(10)$ hours, while BNS systems can take up to weeks. Dedicated fast samplers have been designed to get approximate posteriors on the sky localization to facilitate follow-up electromagnetic observations. Nevertheless, these do not present the whole picture; fast, general parameter estimation therefore remains a primary goal of GW data analysis.

A primary issue with both MCMC and nested sampling is that neither utilizes information about the likelihood's derivative and must therefore randomly walk towards areas of highest likelihood. Derivative based samplers, on the other hand, have been shown to extrapolate well to higher dimensions although they sometimes come with their own drawbacks. Here we simply aim to demonstrate the utility of a derivative based sampler and their efficiency on a small test problem. In particular, we will show that proposals made using an Hamiltonian Monte Carlo (MC) sampler are accepted at a much higher rate than a traditional MCMC algorithm.

For our basic example we perform an injection recovery test on a seven dimensional parameter space with the same three detector network setup considered in § 3.2. More specifically, we generate Gaussian noise consistent with the measured PSDs for each detector and then inject a BBH signal with parameters: $M_c = 23.82 M_\odot$, $\eta = 0.248$, $\chi_1 = 0.3$, $\chi_2 = -0.4$, $D = 1.6$ Gpc, $t_c = 0.0$, and $\phi_c = 0.0$. Using a standard Gaussian likelihood, we then run the HMC sampler implemented in `flowMC` for XX steps. **(TE: Describe more carefully what we do)**

In Fig. 5, the grey contours show the posterior recovered from our injected signal and the orange represents the injected parameters. From the one dimensional histograms along the diagonal, it is clear that we successfully recover all seven parameters. This is expected since the injected binary is relatively nearby.

To illustrate the benefit of a gradient based sampler, we run the same sampling as above but instead use a Gaussian random walk (GRW) sampler. We sample for the same number of steps as used in the HMC with iden-

tical initializations to explore acceptance rates of new points. For the HMC example, find that the mean local acceptance rate across the 15 chains is around ~ 0.28 , where as the local acceptance rate for the equivalent GRW sampler is XXX. Since we are running the chains from the same initialization, this enhanced acceptance for HMC can be mainly associated with use of gradient information to guide sampling. We therefore expect gradient based samplers to converge significantly faster than typical samplers, especially in higher dimensions. In a follow up paper we will demonstrate that minute scale PE can be achieved by combining normalizing flows (Wong et al. 2022; Gabri   et al. 2022), GPU acceleration, and a derivative based sampler (Wong et al. in prep.).

4. DISCUSSION AND CONCLUSION

In this paper we introduced and discussed the various benefits of differentiable waveforms in JAX for GW data analysis. First, we demonstrated the speed and accuracy of our implementation of the aligned spin IMRPhenomD waveform. In particular, we showed that it matches the `lalsuite` implementation to near machine precision and can be easily parallelized on a GPU, making waveform calls up to five orders of magnitude faster. Second, we discussed three data analysis tasks which can all be substantially improved by utilizing derivative information of the waveform. Although we primarily discuss toy examples in this paper, each can be extended to the full data analysis task, some of which will be shown in upcoming papers (Wong et al. in prep.). Differentiable waveforms therefore represent a crucial tool to perform efficient GW science.

Currently the biggest constraint to adopting differentiable waveforms is the need to re-write the most commonly used waveforms into JAX (or pure python). In order to showcase the benefits of differentiable waveforms as quickly as possible, at the time of writing, we have only implemented an aligned spin GW model (IMRPhenomD). We plan on adding a variety of different waveforms to `ripple` in the near future with the primary goal of reaching a JAX version of a fully precessing, higher order mode waveform such as IMRPhenomXPHM. Ideally, future waveforms should be implemented either in pure python or using JAX directly. This would ensure that the community can easily utilize differentiability and hardware acceleration in the future.

In this paper, we have primarily focussed on the IMRPhenom family of waveforms as their closed form expression is perfectly suited for implementation in JAX. Two other waveform families are commonly used in GW data analysis: the effective-one-body (EOB) and numerical

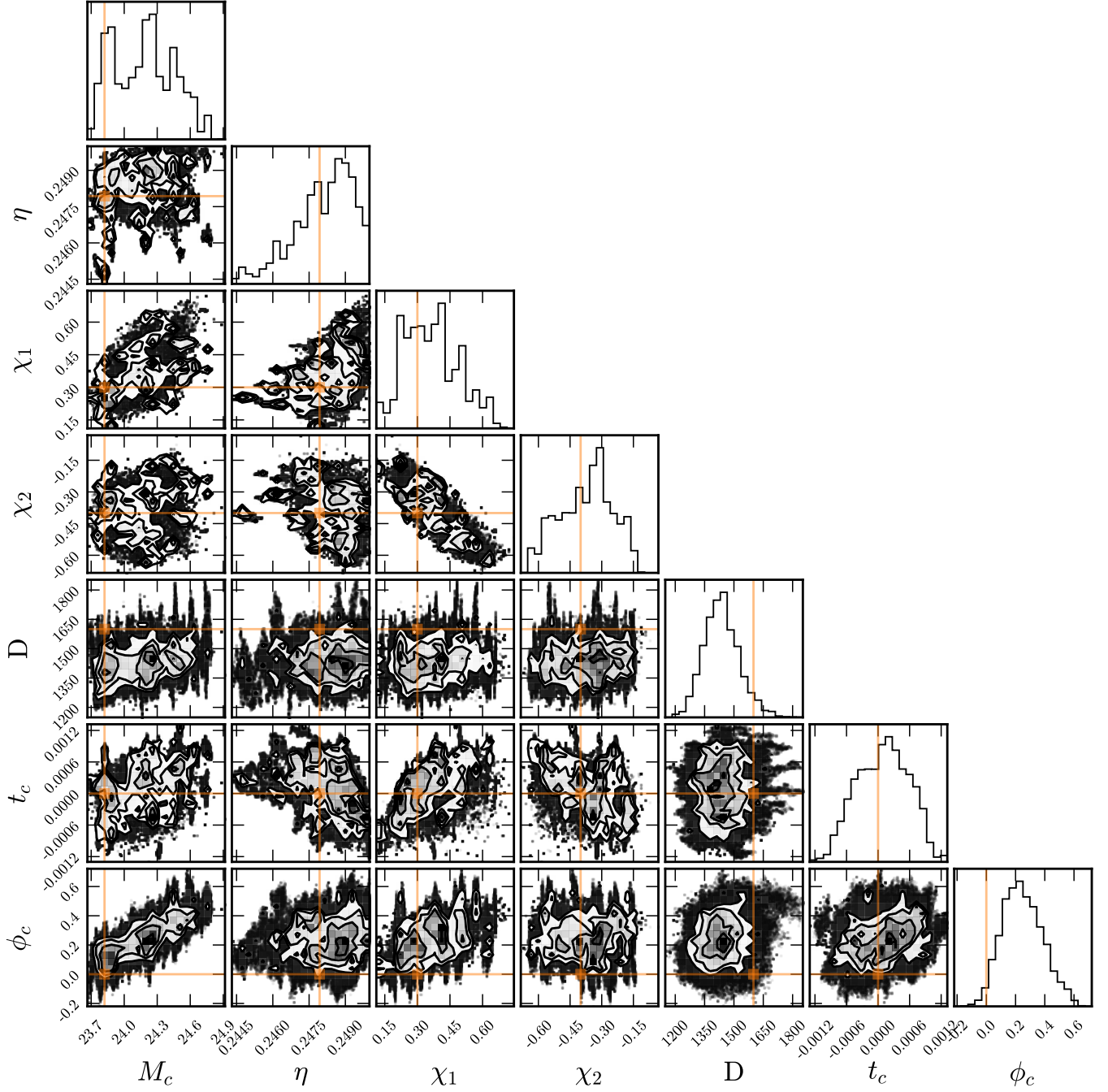


Figure 5. Corner plot

relativity surrogate (NRSurrogate). Some progress has been made towards the construction of a differentiable NRSurrogate, currently it seems difficult to implement EOB waveforms in JAX. In particular, the evolution of the Hamiltonian required to evaluate an EOB waveform is both inherently slow to differentiate and difficult to implement in JAX which requires fixed length arrays for its JIT compilation. Since EOB waveforms are often re-

garded as the state-of-the-art, more work is required to see if a fast, differentiable implementation is possible.

(TE: End on a final good thing?)

5. ACKNOWLEDGMENTS

This work was supported by collaborative visits funded by the Cosmology and Astroparticle Student and Postdoc Exchange Network (CASPEN). T.E. is supported by the Horizon Postdoctoral Fellowship.

REFERENCES

- Abadi, M., Agarwal, A., Barham, P., et al. 2015, TensorFlow: Large-Scale Machine Learning on Heterogeneous Systems. <https://www.tensorflow.org/>
- Abbott, R., et al. 2021. <https://arxiv.org/abs/2111.03606>
- Betancourt, M. 2017, arXiv e-prints, arXiv:1701.02434. <https://arxiv.org/abs/1701.02434>
- Borhanian, S. 2021, *Class. Quant. Grav.*, 38, 175014, doi: [10.1088/1361-6382/ac1618](https://doi.org/10.1088/1361-6382/ac1618)
- Bradbury, J., Frostig, R., Hawkins, P., et al. 2018, JAX: composable transformations of Python+NumPy programs, 0.2.5. <http://github.com/google/jax>
- Coogan, A., Edwards, T., Foreman-Mackey, D., et al. 2022a, ripple, 0.0.1. <https://github.com/tedwards2412/ripple>
- Coogan, A., Edwards, T. D. P., Chia, H. S., et al. 2022b. <https://arxiv.org/abs/2202.09380>
- Feroz, F., Hobson, M. P., & Bridges, M. 2009, *Mon. Not. Roy. Astron. Soc.*, 398, 1601, doi: [10.1111/j.1365-2966.2009.14548.x](https://doi.org/10.1111/j.1365-2966.2009.14548.x)
- Gabrié, M., Rotskoff, G. M., & Vanden-Eijnden, E. 2022, *Proc. Nat. Acad. Sci.*, 119, e2109420119, doi: [10.1073/pnas.2109420119](https://doi.org/10.1073/pnas.2109420119)
- Husa, S., Khan, S., Hannam, M., et al. 2016, *Phys. Rev. D*, 93, 044006, doi: [10.1103/PhysRevD.93.044006](https://doi.org/10.1103/PhysRevD.93.044006)
- Iacovelli, F., Mancarella, M., Foffa, S., & Maggiore, M. 2022a. <https://arxiv.org/abs/2207.02771>
- . 2022b. <https://arxiv.org/abs/2207.06910>
- Innes, M. 2018, CoRR, abs/1810.07951. <https://arxiv.org/abs/1810.07951>
- Khan, S., Husa, S., Hannam, M., et al. 2016, *Phys. Rev. D*, 93, 044007, doi: [10.1103/PhysRevD.93.044007](https://doi.org/10.1103/PhysRevD.93.044007)
- Owen, B. J. 1996, *Phys. Rev. D*, 53, 6749, doi: [10.1103/PhysRevD.53.6749](https://doi.org/10.1103/PhysRevD.53.6749)
- Owen, B. J., & Sathyaprakash, B. S. 1999, *Phys. Rev. D*, 60, 022002, doi: [10.1103/PhysRevD.60.022002](https://doi.org/10.1103/PhysRevD.60.022002)
- Paszke, A., Gross, S., Massa, F., et al. 2019, in *Advances in Neural Information Processing Systems* 32, ed. H. Wallach, H. Larochelle, A. Beygelzimer, F. d'Alché-Buc, E. Fox, & R. Garnett (Curran Associates, Inc.), 8024–8035. <http://papers.neurips.cc/paper/9015-pytorch-an-imperative-style-high-performance-deep-learning-library.pdf>
- Revels, J., Lubin, M., & Papamarkou, T. 2016, arXiv:1607.07892 [cs.MS]. <https://arxiv.org/abs/1607.07892>
- Speagle, J. S. 2020, *MNRAS*, 493, 3132, doi: [10.1093/mnras/staa278](https://doi.org/10.1093/mnras/staa278)
- Wong, K. W. K., Breivik, K., Farr, W. M., & Luger, R. 2022. <https://arxiv.org/abs/2206.04062>
- Wong, K. W. K., Gabrié, M., & Foreman-Mackey, D. 2022, arXiv e-prints, arXiv:2211.06397. <https://arxiv.org/abs/2211.06397>
- Wong, K. W. K., Isi, M., & Edwards, T. D. P. in prep.